UC San Diego
UC San Diego Previously Published Works

Title

Modulating the bistable potential energy separatrix for augmented broadband vibration energy harvesting

Permalink

https://escholarship.org/uc/item/3mv9m0h3

Journal

Journal of Intelligent Material Systems and Structures, 28(3)

ISSN

1045-389X

Authors

Ouellette, Scott A
Todd, Michael D

Publication Date

2017-02-01

DOI

10.1177/1045389x16634210

Peer reviewed

Modulating the bistable potential energy separatrix for augmented broadband vibration energy harvesting

Scott A Ouellette and Michael D Todd

Department of Structural Engineering, University of California, San Diego, USA

Abstract

In recent years, increased interest in broadband vibration energy harvesting (VEH) schemes has been a main topic of interest among researchers. One of the most successful approaches towards broadband vibration energy capture has been with bistable inertial generators. These devices leverage a nonlinear restoring force to exploit the hardening spring response to increase the resonant frequency bandwidth beyond the characteristically narrowband resonant frequency associated with conventional linear inertial generators. However, one issue with bistable energy harvesters is the presence of low-amplitude oscillations whose energy is insufficient to overcome the potential energy separatrix barrier between the competing potential wells. This paper presents the effects of controlling the magnitude of the potential energy separatrix by means of a high-permeability electromagnet in order to increase the resonant response bandwidth for low-amplitude harmonic excitations. An analytical model of the bifurcation space resulting from two control parameters is presented along with an experimental validation study. Lastly, an open-loop control law is developed and tested to validate the resonant frequency bandwidth augmentation for harmonic chirp excitations.

Introduction

Broadband VEH techniques have been a significant domain of research in recent years as a pragmatic means of vibration energy capture in more realistic environments where the frequency content of excitation sources is often broadband, non-stationary, and stochastic. In attempts to achieve broadband resonance, researchers have investigated several tuning methods to increase the resonance bandwidth of vibration-based energy harvesters. Erturk and Elvin (Elvin and Erturk, 2013) classify the tuning methods as either manual tuning (i.e., operator intervention is required) or self-tuning. While manual tuning is technically a low-power solution, the implementation is sub-optimal for field deployment due to the necessity of human intervention. Self-tuning methods are much more attractive for remote energy harvesting applications as the device could potentially provide autonomous power to a sensor node (or system) well beyond the functional lifetime of a conventional battery. It should be noted that an essential criterion for self-tuning methods to be feasible for vibration energy harvester designs is that they generate a net-positive power output.

Investigations into nonlinear dynamics-based approaches for broadband vibration energy harvesting have garnered increasing interest in the past few years (Friswell et al., 2012; Litak et al., 2010; Zhu and Beeby, 2013). While various system designs have been investigated, this paper will focus on exploiting the nature of bistable oscillators.

Bistable configurations have been demonstrated to exhibit many favorable resonance response characteristics as a passive means of broadband energy capture (Erturk and Inman, 2011; Gao et al., 2014; Liu et al., 2013; Stanton et al., 2010; Su et al., 2014; Zhu and Zu, 2014). In these configurations, a mechanical nonlinearity is induced on an inertial generator, and the resulting response resembles that of a Duffing oscillator. However, due to the nature of the nonlinear system dynamics, there exists a set of low-energy responses resulting from the competing inertial forces of the tip mass and the bistable well separatrix (Virgin et al., 1992). For many bistable energy harvesters, the double-well restoring potential is generated by means of magnetic
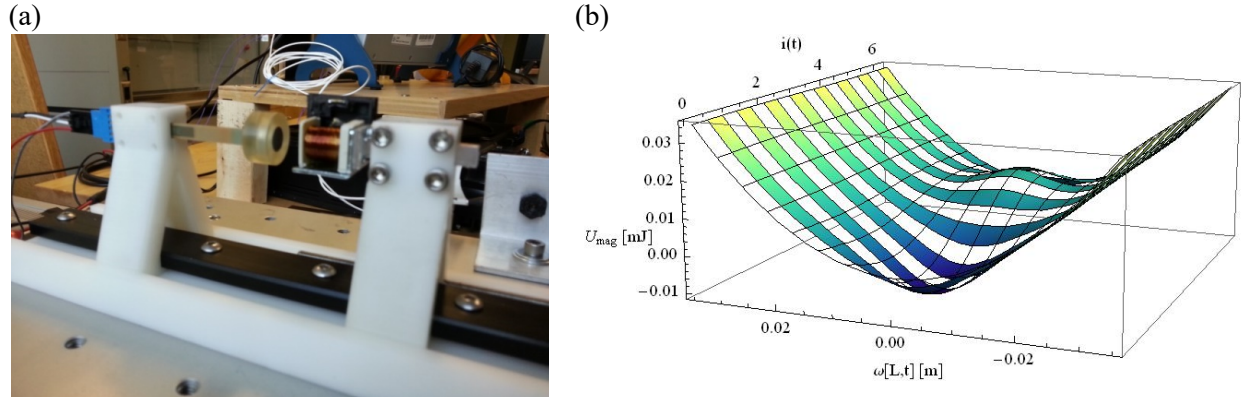
Figure 1. (a) Experimental setup of modulated inertial generator (MIG) energy harvester, and (b) analytically derived time-varying total potential energy function of the MIG energy harvester.

repulsion, while other approaches used in developing a bistable potential have been via a compressed buckled beam and magnetic attraction (Harne and Wang, 2013). In general, manual tuning is required to adjust the nonlinear response of these systems, which can be a hindrance for field operations.

New approaches towards passive self-tuning of bistable inertial generators have been investigated as a means of expanding the broadband resonance response (Gao et al., 2014; Leng et al., 2015) through the use of an elastic support mechanism for the buckling magnet. The concept proposed in this paper is to actively manipulate the bistable potential separatrix by adaptively changing the current direction within a high-permeability electromagnet. By altering the coil current direction, the electromagnet polarity can be controlled, allowing for the potential energy of the system restoring force to fully transition between monostable and bistable, as shown below in Figure 1(b).

The following sections of this paper will present analytical models for the modal response and critical buckling loads of the composite inertial generator, closed-form expressions for the nonlinear magnetic potential energy due to a permanent magnet interacting with a high-permeability electromagnet, and an analytical 2-parameter bifurcation diagram of the design space that yields a bistable system restoring force. Furthermore, experimental tests are employed to validate the analytical models and confirm the hypothesis that adaptive control of the bistable separatrix barrier can lead to an augmented broadband resonant response bandwidth for low-amplitude harmonic excitations.

## Quasi-static buckling analysis and modal model

In this section, analytical models for the global buckling mode and primary bending mode are developed in order to determine approximate values of interest (e.g., buckling load and natural frequency) for the sections that follow. Additionally, a finite element model was developed to verify the analytical modal model results with regards to the estimated natural frequency for various tip mass values. The inertial generator used in the experimental tests is the V22BL (Midé Corporation) Volture™ piezoelectric energy harvester, with the experimental natural frequency values for various tip masses provided by the manufacturer were used as a means of modal model validation.

Analytical and numerical modal analysis

The analytical modal model developed to study this inertial generator with an added tip mass follows the procedure outlined by Koplow et al. (Koplow et al., 2006) and Stanton and Mann (Stanton and Mann, 2010) for beams with step changes in cross section. In this study, the composite beam is parsed into three sections, each with unique bending stiffness properties. Figure 2 shows a layered diagram of the composite beam stacking sequence, consisting of the four materials that comprise the laminate in a relative scale of their respective thicknesses. To reduce the model
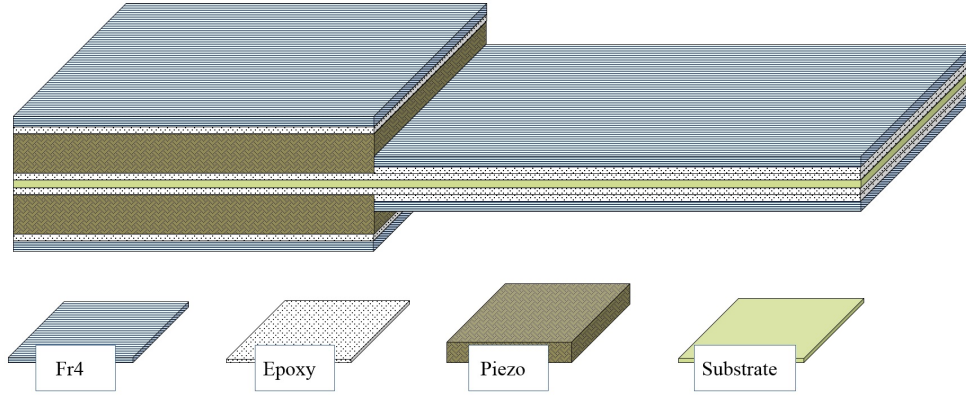
Figure 2. Laminate stacking sequence of Midé V22BL inertial generator.
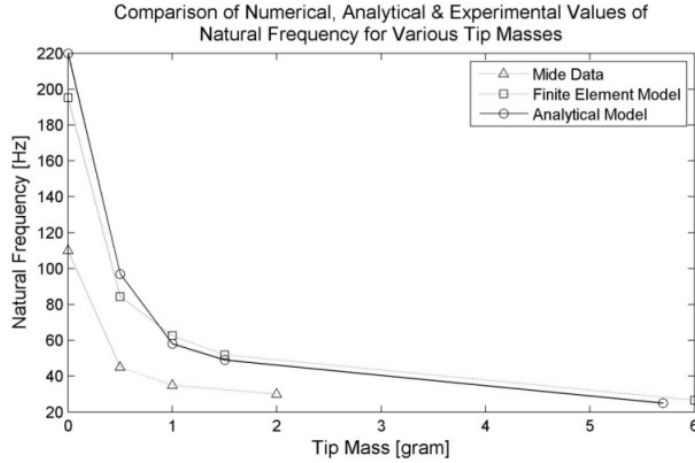
Figure 3. Comparison of analytical and finite element models of the V22BL inertial generator to experimental values provided in the manufacturer datasheet.

complexity often encountered with composite beams, each section is treated as an isotropic prismatic Euler-Bernoulli beam, with the elastic modulus calculated as the average modulus for each section in the following manner:

$$E_1 = \frac{E_s A_s + E_p A_p + E_{fr4} A_{fr4} + E_e A_e}{A_s + A_p + A_{fr4} + A_e} \quad (1)$$

where, $A_{\square}$ represents the total cross-sectional area of each respective lamina. The specific values used for each lamina are detailed in Table 1. The tip mass was modeled as an isotropic cylinder (non-rigid), with the diameter kept as a variable in order to adjust the overall mass load for the model comparison study.

For the finite element model, the beam was again parsed into three sections and modeled using linear-quadrilateral and triangular shell elements, with a mean element size of 1 mm. The only variation between the analytical model and the finite element model is the treatment of the tip mass, in that for the finite element model the geometric properties and moment of inertia were idealized as a distributed mass load on the edge elements.

Both the analytical model and finite element model assumed an idealized fixed-end condition at the beam root, keeping with the intended application of traditional inertial generator configurations. Comparing the resulting estimations for the primary natural frequency to the experimental values provided by the manufacturer shows each model to have relatively

Table 1
Elastic and geometric properties used in composite beam analysis

Substrate Properties		
Parameter	Symbol	Value
Modulus	E_s	2.41 Gpa
Thickness	t_s	0.1 mm
Width	b	6.1 mm
Length	L_s	53.16 mm
Density	ρ_s	1290 kg/m^3
Piezoelectric Layer Properties		
Modulus	E_p	63 Gpa
Thickness	t_p	0.254 mm
Width	b_p	3.81 mm
Length	L_p	22.86 mm
Density	ρ_p	7700 kg/m^3
Fiberglass (FR-4) Properties		
Modulus	E_{fr4}	24.8 Gpa
Thickness	t_{fr4}	0.039 mm
Density	ρ_{fr4}	1920 kg/m^3
Epoxy Resin Properties		
Modulus	E_e	1.4 Gpa
Thickness	t_e	2.54 μm
Density	ρ_e	1420 kg/m^3
Tip-Mass Properties		
Mass	m_m	5.7 g
Diameter	d_m	19.05 mm
Length	l_m	9.525 mm
Density	ρ_m	1927 kg/m^3

strong agreement to each other, while overall predicting a stiffer beam. However, the models qualitatively predict the asymptotic convergence to a natural frequency of approximately 25 Hz for tip mass values greater than 2 grams, as shown in Figure 3. For the experimental tests conducted, the tip mass was measured as 5.7 grams, with a measured damped natural frequency of 25.27 Hz. For both models with a 5.7 gram tip mass, the estimated natural frequency was calculated at 25.02 Hz and 26.64 Hz for the analytical and finite element approach, respectively.
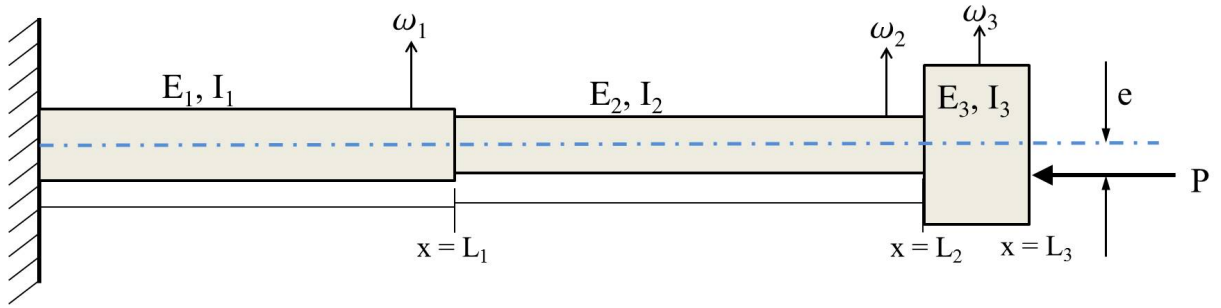
Analytical buckling analysis

An analytical static buckling model was also derived for the inertial generator independent of the exact description of the magnetic repulsion forces used to generate the nonlinear restoring potential. The insights gained by studying the global buckling of the beam with an offset eccentricity tuning parameter were instructive in realizing the effective range of mechanical point loads required for generating a bistable potential function. The model approach used in this buckling analysis is nearly identical to the analytical modal model, with the chief difference being the equation

of shape due to the presence of an externally applied load as shown in Figure 4. The governing ordinary differential equation for the deformed shape of the beam is as follows:

$$\frac{\partial^4 \omega_i}{\partial x^4} + \lambda_i^2 \frac{\partial^2 \omega_i}{\partial x^2} = 0 \qquad (2a)$$

$$\lambda_i^2 = \frac{P}{E_i I_i} \qquad (2b)$$

where, λ_i is the non-dimensionalized buckling parameter, and ω_i represents the lateral deflection for each section, with $i = 3$ sections. Equation (2a) assumes for there are no externally applied lateral loads, and that there are no beam imperfections. A general solution to this problem can be found in (Virgin, 2007). Similar to the modal analysis approach developed by Koplow (Koplow et al., 2006), the displacement, rotation, shear, and moment at each section interface must be set equivalent to ensure continuity in the deflected shape. However, since this model includes an eccentric offset parameter (e), a non-zero moment arm manifests at the beam tip, which must be accounted for in the boundary condition. As such,

Figure 4. Analytical buckling model with tunable eccentric load.
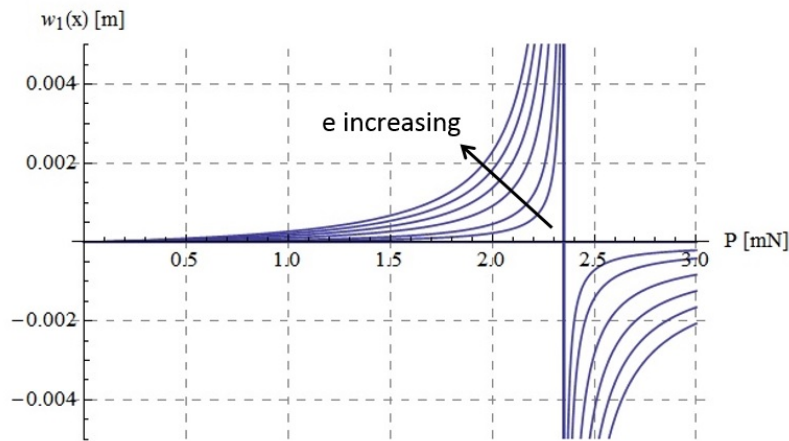
Figure 5. Buckling diagram for piezoelectric beam section as a function of increasing eccentricity (e).

the moment equilibrium boundary condition at the beam tip is as follows:

$$\frac{\partial^2 \omega_3(x=L_3)}{\partial x^2} = \lambda_3^2 e \qquad (3)$$

Combining all boundary and compatibility conditions results in a 12x12 matrix set of equations with a non-zero right-hand side resulting from the eccentrically applied buckling load.

Since energy is only produced in the inertial generator for strain fields in the piezoelectric layers, this investigation is primarily focused on the buckling loads for beam section 1 (nearest the beam root). Figure 5 shows the deflection evaluated for $\omega_1(x = L_1)$ as a function of applied load for varying eccentricity values. The critical buckling load for the modeled composite beam, which assumes perfect load alignment by setting the eccentricity value to zero, is calculated as 2.33 mN. Once an imperfection/eccentricity is introduced to the framework, the critical

bifurcation load is no longer an explicit point, and is generally perceived as the point in which the lateral deflection makes a sharp "knee" bend. Of particular interest in this study is the apparent convergence of eccentrically applied buckling load values. Assuming an experimental misalignment of the magnets of 2 mm will only result in a 5.6% reduction in critical buckling load required to generate the bistability.

Electromagnet dipole moment and bifurcation diagram

Now that the critical buckling load for the inertial generator has been established, it is instructive to model the force interaction between the two interacting magnets. A vector-gradient method for approximating the force between to interacting magnetic dipoles in free-space was proposed by Yung et al. (Yung et al., 1998), and later applied to the study of bistable energy harvesters by Stanton
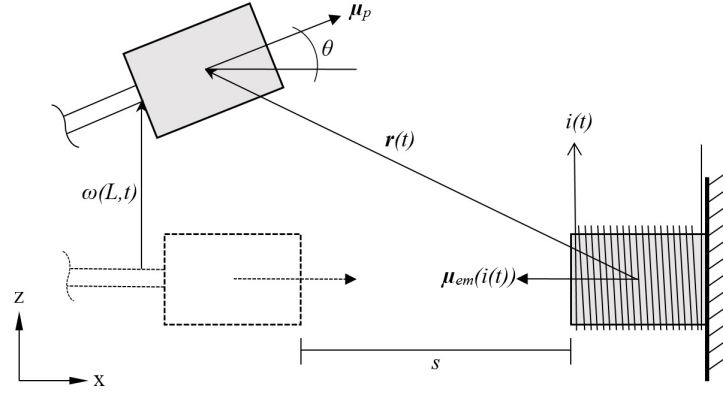
Figure 6. 2D geometric diagram of the magnetic dipole moment interaction.

et al. (Stanton et al., 2010). In essence, this approach defines the magnetic potential energy field in the 2D plane as the inner product of the magnetic flux density of the interacting dipole moments ($B_{p\text{-}em}$) with the stationary buckling magnet (μ_{em}). Figure 6 shows a simplified diagram of the interacting magnetic dipoles with respect to the Cartesian reference frame, with the permanent magnet affixed to the beam tip and the electromagnet held stationary. For cylindrical permanent magnets, a first-order approximation of the dipole moment (μ_p) can be expressed as follows:

$$\vec{\mu}_p = \frac{B_r}{\mu_0} \pi r_p{}^2 h_p \qquad (4)$$

where B_r represents the remnant flux density of the ferroelectric material after the magnetizing field is removed, μ_o is the permeability of free space, and r_p and h_p are the cylinder radius and height, respectively. A cursory analysis of equation (4) reveals the magnitude of the dipole moment is approximately proportional to its volume and remnant flux density. To fully define the magnetic potential energy, U_m, it is necessary to derive an expression for the dipole moment of the stationary electromagnet.

In order to derive an approximate expression for the dipole moment produced by a finite length cylindrical electromagnet, this study employs analytical methods from classical physics in combination with a magnetic circuit modeling approach for high-efficiency transformer design. Since the electromagnet used in this study is

cylindrical in shape, it is assumed that the dipole moment can be approximated as similar to that of a permanent magnet, with the notable variation being the flux density (B) is a function of the coil current, as shown below in equation (5).

$$\vec{\mu}_{em} = \frac{B(i(t))}{\mu_0} \pi r_{em}{}^2 h_{em} \qquad (5)$$

Magnetic dipole moment model for a cylindrical solenoid

A framework for analyzing the flux density field of a finite length solenoid (i.e. an air-cored electromagnet) was developed by Derby & Olbert (Derby and Olbert, 2010), and was applied towards the analysis of an electromagnet by Ouellette and Todd (Ouellette and Todd, 2014).

The addition of an iron core to the solenoid has two notable effects: 1) the magnetic field generated per unit of coil current increases greatly due to the alignment of magnetic domains within the ferromagnetic material, making special note that the relative permeability of soft iron cores is in the range of 10^3-10^5, and 2) the field direction is focused within the boundary of the core. Unlike air, an iron core has a finite set of magnetic domains, and thus will saturate at a flux density level that is proportional to the molecular chemistry of the material and the core volume. When the magnetizing current is reduced to zero, the iron core still remains magnetized, and thus the material exhibits a hysteretic relationship between the two fields. It is important to note that once a
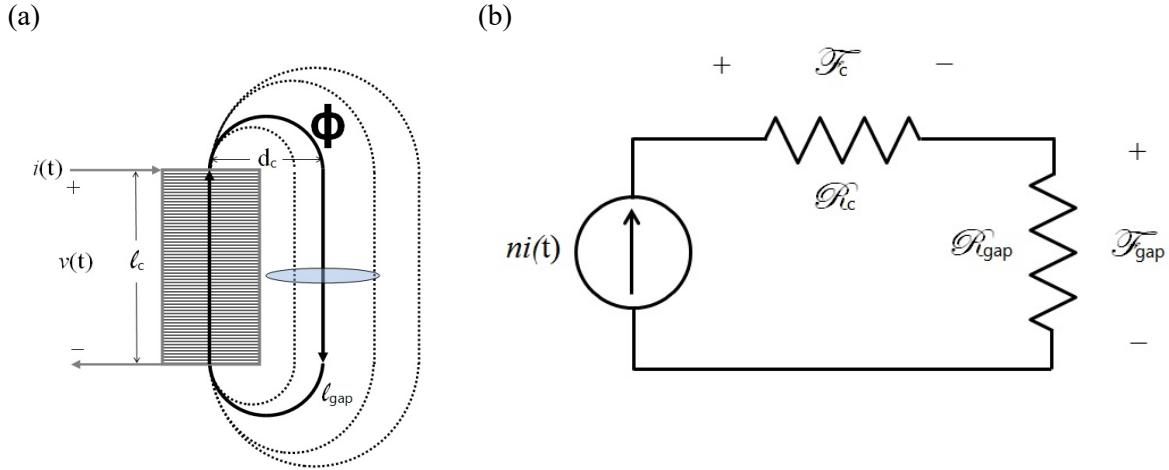
Figure 7. (a) Diagram of a cylindrical electromagnet with an assumed magnetic field path (ϕ) shown, (b) an equivalent magnetic circuit accounting for the air gap reluctance, $\mathcal{R}_{gap}$.

magnetizing field is applied to the core, it will only return to a de-magnetized state if it is heated to its Curie temperature. For this study, the core characteristics are idealized such that the relationship is piecewise linear; a conventional assumption for high- permeability core materials due to their characteristically low coercive force.

Now that a foundation for the electromagnet behavior is established, the focus will shift to deriving an approximate expression for the magnetic dipole moment ($\boldsymbol{\mu}_{em}$) generated by a cylindrical electromagnet, as depicted below in Figure 7(a). To do this, we must first establish principles of magnetic circuits to account for the effect of the open loop. A fundamental principle of electromagnet analysis is that the magnetic field forms a closed loop from one pole to the other. For a simple toroidal inductor, the path is completed by the core, and thus the field strength, $H(t)$, can be assumed to be uniform. The magneto-motive force (MMF), $F_{MM}(t)$, between two points, x_1 and x_2, is simply the integral of the **H**-field between the points. Thus, for a uniform **H**-field, the MMF is: $F_{MM} = H\ell$, where ℓ is the distance between points. Additionally, the total magnetic flux, $\phi(t)$, is the sum of all flux density vectors through a surface, A_c. Therefore, a uniform flux density through a surface with area, A_c, yields the expression: $\phi(t) = \boldsymbol{B}A_c$.

The effect of the air gap can be modeled using an equivalent magnetic circuit model, as shown in Figure 7(b). The essential assumptions for a magnetic circuit using an analog of Kirchhoff's node laws are as follows:

- The divergence of **B** = 0;
- Flux lines are continuous with no end;
- Total flux entering a node must be zero;
- The magnetic force and flux are uniform through an element with cross-sectional surface area, A_c (added for completeness).

For the given essential assumptions, the application of Ampere's Law to the magneto-motive force places a restriction that the **H**-field is evaluated over a closed path. In the previous subsection, it was shown that the magnetic flux path is elliptical. However, for simplicity, the mean magnetic flux path for the solenoid shown in Figure 7(a) assumes a semi-circular rotation with a diameter equivalent to the core diameter. Applying the rules listed above to the system shown in Figure 7(b), the following expression for Ampere's Law is derived:
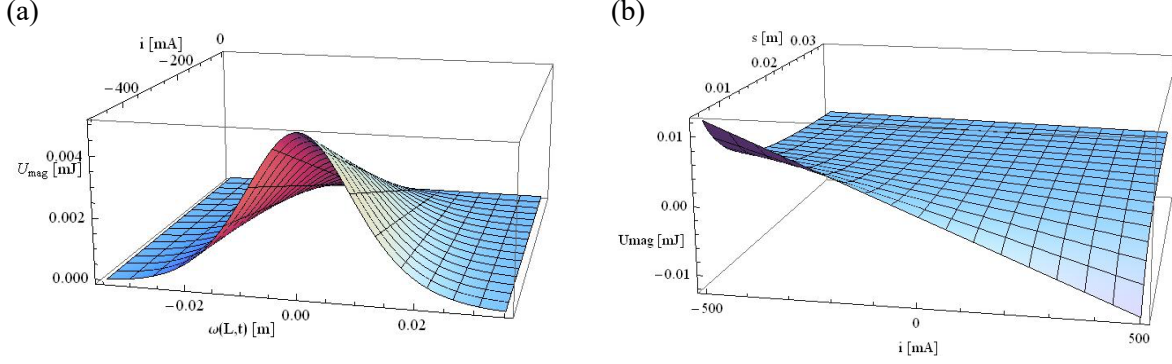
$$ni = \phi(\grave{R}_c + \grave{R}_{gap}) \tag{6a}$$

$$\grave{R}_c = \frac{l_c}{\mu\, A_c} \tag{6b}$$

$$\grave{R}_{gap} = \frac{l_{gap}}{\mu_0 A_c} = \frac{l_c + \pi d_c}{\mu_0 A_c} \tag{6c}$$

Applying equations (6a-c) to equation (5), and assuming a cylindrical electromagnet with an

Figure 8. (a) Nonlinear magnetic potential energy for fixed magnet spacing (s = 10.7 mm) and tip rotation (θ = 0), and (b) relationship of potential energy magnitude and for varying magnet spacing and coil current for perfect magnet alignment (i.e. α = 0, and θ = 0).

ideal iron core, yields the following expression for the magnetic moment:

$$\vec{\mu}_{em} = \frac{n\pi r_c^2 h_c}{\mu_0 A_c \left(\frac{l_c}{\mu A_c} + \frac{l_c + \pi d_c}{\mu_0 A_c}\right)} \begin{cases} i(t) \ for \ |H| < {B_{sat}}/{\mu} \\ I_{sat} \ for \ H \geq {B_{sat}}/{\mu} \end{cases}$$

(7)

Electromagnet power analysis

A cursory analysis of equation (7) shows the large effect on the air gap significantly increases the saturation current. As such, the required number of coil turns, *n*, increases greatly to offset the air gap reluctance. However, there are two issues associated with increasing the number of coil turns that lead to diminishing returns: 1) for a finite cylinder height, h_c, the increasing number of turns will require coil overlap which results in increased coil diameter, and 2) the increased coil length adds to the parasitic resistance, which thus requires a higher terminal voltage, and higher DC power loss due to joule heating.

For most applications of electromagnets, there are two main sources of power loss: 1) DC copper loss/joule heating, and 2) core hysteresis loss. Since core hysteresis loss primarily occurs during high frequency switching applications, its effects are considered to be negligible in the context of this study. The effect of Joule heating on the power loss is of primary concern in this study due to the manner in which the electromagnet is employed. Furthermore, in order for this approach

to be a viable technique in field operations, its effects must produce a net-positive output power. Therefore, analysis of the primary type of power loss is essential in characterizing the device performance, as well as providing a metric for optimization with regard to future design considerations such as material and geometric properties of the ferromagnetic core and wire coil.

The conventional description of Joule heating is to treat the wire coil as a resistor, in which case the power loss is simply $I^2 R_{wire}$, where the wire resistance for a cylindrical coil can be approximated as:

$$R_{wire} = \frac{4\rho_{wire} d_{coil} n}{d_{wire}^2}$$

(8)

where d_{coil} represents the coil diameter, d_{wire} is the wire cross section diameter, and *n* is the total number of coil turns. The maximum buckling force for a set separation distance becomes limited by the saturation current of the core; thus, the DC power loss in the electromagnet occurs at the saturation current level, which can be determined explicitly via equation (7). Solving equation (7) for I_{sat} in terms of B_{sat} yields the upper bound of the DC power loss:

$$(P_{loss})_{DC} = \frac{\left[B_{sat} A_c (\check{R}_c + \check{R}_{gap})\right]^2 \rho_{wire} d_{coil}}{n d_{wire}^2}$$

(9)

Effectively, the optimal electromagnet design, in terms of minimal power loss, will use a relatively large gauge wire, a high-permeability core material, and a small core diameter. This
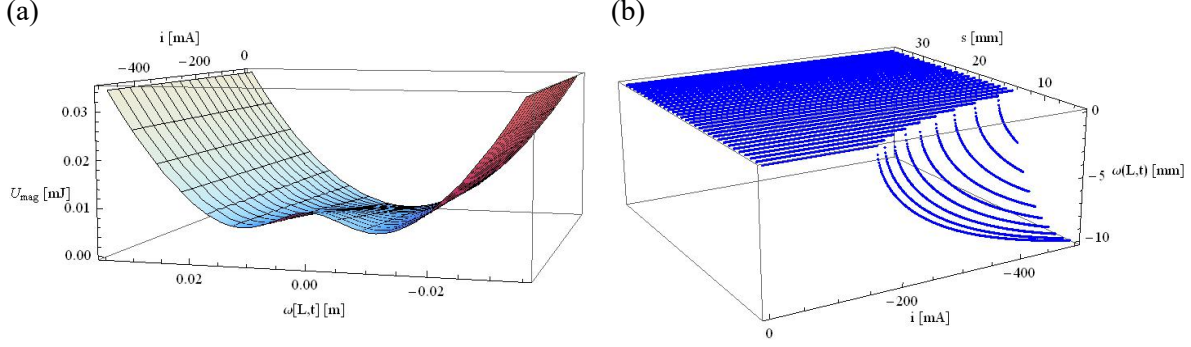
Figure 9. (a) Nonlinear potential energy function with respect to the lateral displacement of the beam tip and an externally applied electromagnet coil current, and (b) the analytical 2-parameter bifurcation diagram for various magnet spacing and coil current values.

model does assume a singular layer coil, so there are higher-order layering effects that are unaccounted for in terms of total wire length and magnetic field gap reluctance estimation. Analytically modeling the nonlinear magnetic potential interaction and its effects on the parametric bifurcation space of the inertial generator is the subject of the next section.

Analytical 2-parameter bifurcation diagram for electromagnetic buckling

A closed-form analytical approximation of the magnetic dipole moment for a cylindrical electromagnet was derived in equation (7) in the previous section. Applying the expression in equation (7) to the expression for magnetic potential energy found in Stanton et al. will generate the closed-form expression for the nonlinear magnetic potential function. Due to the complexity of the calculations, the symbolic manipulation software MATHEMATICA was used to derive the full nonlinear magnetic potential energy, which is listed in full in the Appendix.

Since magnitude of the potential energy is a function of 4 variables, only specific cross sections of the data can be visualized. Figure 8 shows two such visualizations of the magnetic potential function for various configurations of fixed and variable parameters. Of particular relevance to the bifurcation study is the comparison of the potential energy magnitude for varying spacing and coil current values Figure 8(b). This figure shows the highly nonlinear relationship between the magnetic potential and the magnet spacing, whereas, with respect to the coil

current, the magnetic potential is roughly linear. In order to generate the bifurcation diagram, it is first necessary to evaluate the total potential energy present in the modulated inertial generator (MIG) system. Keeping consistent with the energy description of the system, the elastic strain energy along the axial direction for a prismatic beam is expressed as follows:

$$U_S = \tfrac{1}{2} E_S I_S \int_0^L [\omega''(x,t)]^2 \, dx \qquad (10)$$

where, $E_S I_S$ represents the bending stiffness for an isotropic prismatic section, and $\omega(x,t)$ is the lateral displacement at any point (x) in the beam for all time (*t*). A common approach for analyzing continuous Euler-Bernoulli beams is to separate the temporal and spatial variables via a modal - expansion consisting of a finite sum of orthogonal mode shapes and generalized temporal displacements. By applying a modal expansion of the form $\omega(x,t) = \Sigma \, \alpha(t) \, \phi(x)$, the expression in equation (10) reduces to a simple quadratic function with respect to the temporal displacement parameter $\alpha(t)$.

$$U_S = \tfrac{1}{2} E_S I_S \Phi \alpha(t)^2 \qquad (11a)$$

$$\Phi = \int_0^L \phi''(x)^2 \, dx \qquad (11b)$$

where $\phi(x)$ is the composite mode shape developed in section 3.1. Since this beam is electromechanically coupled through the piezoelectric layers, it is also necessary to account for the bending enthalpy for each layer within the
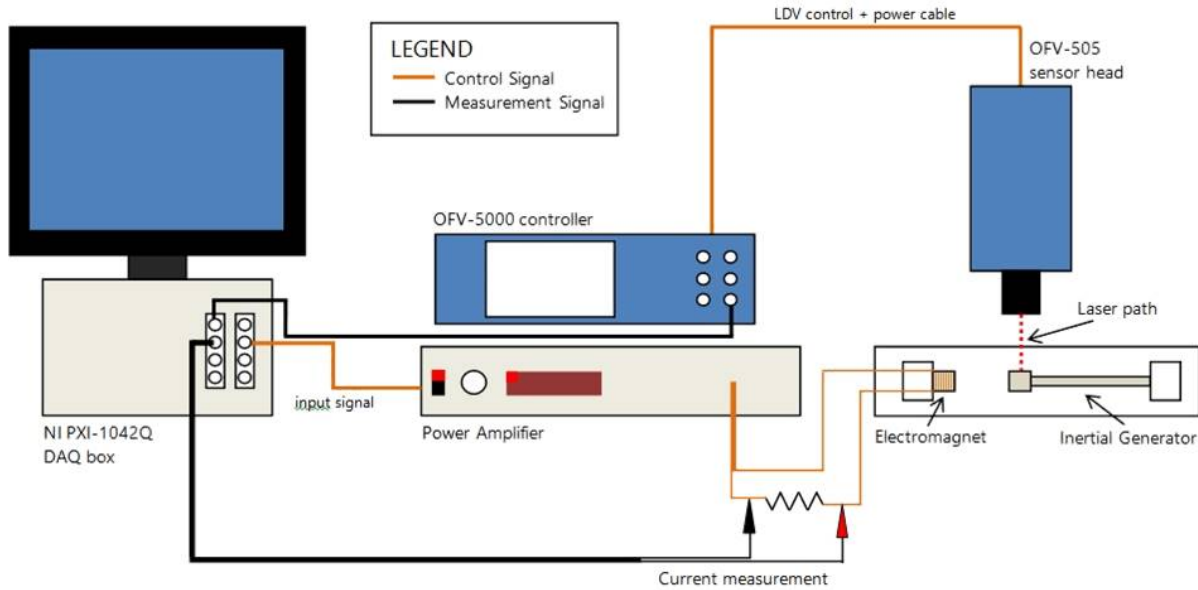
Figure 10. Diagram of 2-parameter bifurcation experimental setup.

elastic strain energy formulation. A method for evaluating the bending enthalpy was presented by Stanton et al. and does not require further review with regards to the intent of this investigation (Stanton et al., 2010). Summing the three potential energy functions gives the total system restoring potential, of which the nonlinear restoring force (Ψ) can be derived by means of a partial derivative with respect to the generalized temporal displacement $\Psi = \partial U_{total}/\partial\alpha(t)$.

Figure 9(a) shows the evaluation of the total potential energy function as the coil current parameter is varied, and in it we see the parabolic function smoothly transition into a bistable potential well system. For a system in which the magnets are initially perfectly aligned, the bifurcation diagram is reduced to a function of two parameters: magnet spacing (s) and coil current (i_{coil}). As such, evaluating the critical points of the nonlinear restoring force (Ψ) for various parametric values of spacing and current yields the 3D bifurcation diagram shown in Figure 9(b).

Experimental results

This section describes the experimental tests used to validate the theoretical and analytical models presented in the previous sections. The primary objectives of the tests performed were to quantitatively validate the analytical 2-parameter

bifurcation diagram, investigate the bandwidth response of the inertial generator subject to a range of buckling loads, and to confirm the initial hypothesis that the resonant response bandwidth can be augmented by modulating the buckling force in real time during a test.

Experimental validation of parametric bifurcation space

A picture of the modulated bistable energy harvester experimental setup is shown in Figure 1(a). As stated in section 3, the inertial generator used in these experiments is the Midé V22BL. A cylindrical tip mass of polysulfone was fabricated to mount to the tip of the inertial generator, and a 3/8" diameter by 3/16" deep center bore was implemented to embed the permanent tip magnet

Table 2

Properties of tip magnet and electromagnet

Electromagnet properties		
Parameter	Symbol	Value
Core length	l_c	13.8 mm
Core diameter	d_c	9.53 mm
Number of coil turns	n	1000
Core permeability	μ	2.9×10^6 N/A^2
Permeability of free space	μ_o	4.9×10^{-7} N/A^2
Tip magnet properties		
Length	l_m	4.76 mm
Diameter	d_m	9.53 mm
Remnant flux density	B_r	1.48 T
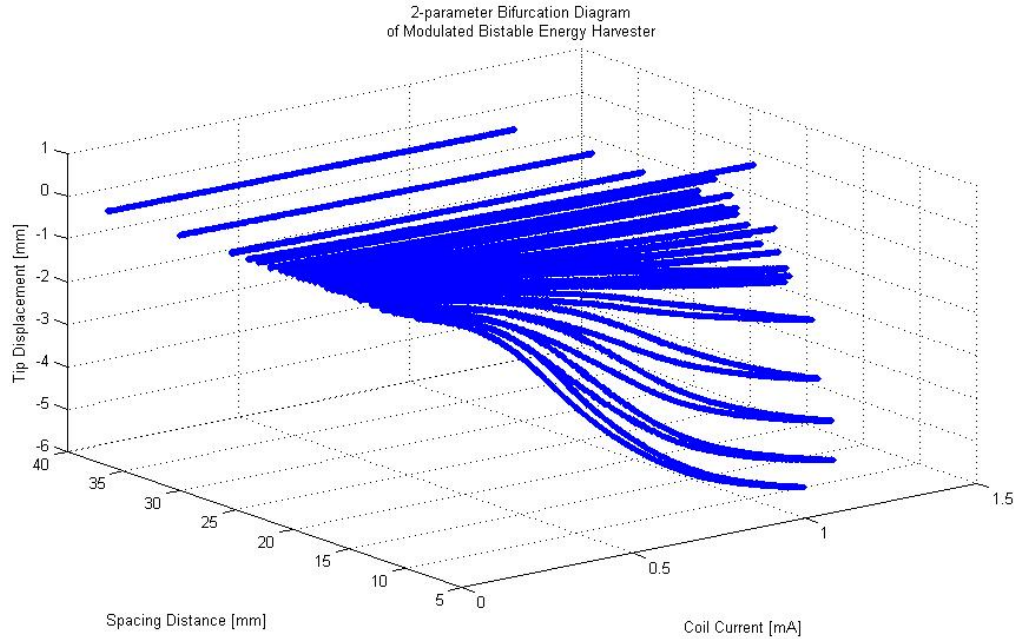
Figure 11. Experimental 2-parameter bifurcation diagram

(D63-N52, K&J Magnetics). A cart and track system was fabricated out of Delrin to allow for variable magnetic spacing, which was controlled by a stepper motor for accurate spacing tolerances. The electromagnet used is an automotive relay (LD-5F-R, Raylex Elec.) with the protective plastic shell and switch contacts removed.

Figure 10 is a diagram of the experimental setup used to validate the analytical 2-parameter bifurcation diagram. A high resolution Laser-Doppler Vibrometer (OFV 505/5000, Polytec Inc.) was used to measure the lateral displacement of the end mass on the inertial generator. A National Instruments PXI-1042Q data acquisition system was used with LabVIEW to generate the triangle wave excitation signal that cycled from 0-1 A of coil current with a frequency of 0.05 Hz.

A total of 26 trials were conducted over a magnet spacing range of 9 – 36.35 mm, with the results of these tests shown in Figure 11. Comparing the results to the analytical bifurcation diagram in Figure 9(b) shows a strong quantitative correlation of the initial bifurcation coil current, as well as the spatial dependence. Qualitatively there are two main differences between the analytical and experimental bifurcation diagrams are the result of the modeling assumption of a lossless core material (no hysteresis), and perfect magnet
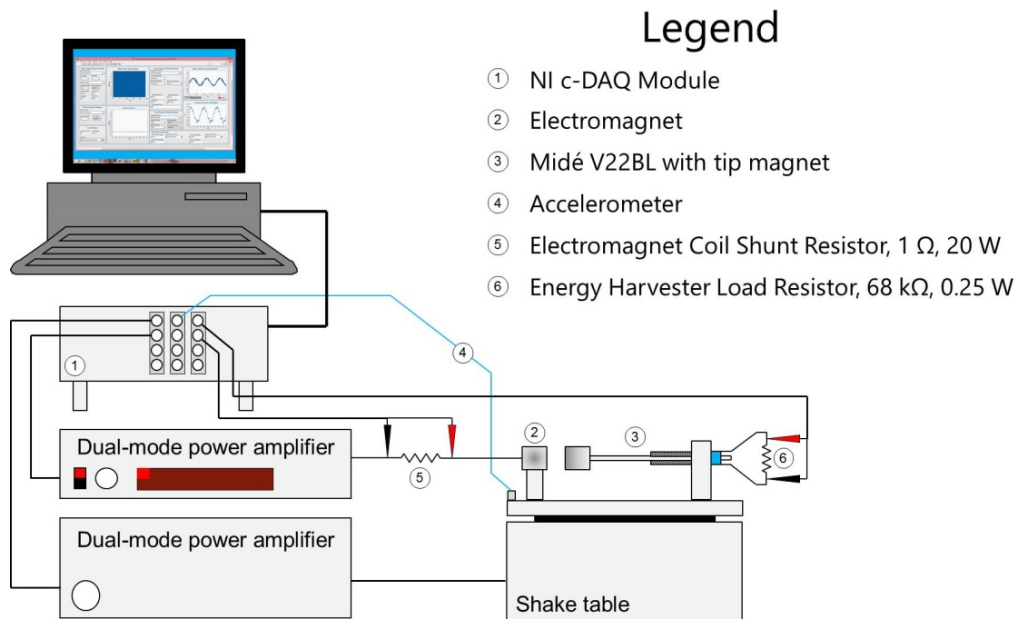
alignment. As seen in Figure 11, there is a clear hysteretic effect on the bifurcation when the current ramps back down from the initial charge.

Parametric investigation of broadband response

This section will review the parametric power output of the nonlinear energy harvester subject to harmonic chirp excitations of amplitude 0.25 g with a sweep rate (ω_r) of 0.1 Hz/s. The parametric study consisted of 40 trials in with the magnet spacing held to a fixed separation distance, and the electromagnet coil current set to a fixed current for the duration of each chirp excitation. Between each trial, the coil current was marginally increased from 0 mA up to a max of 400 mA.

The experimental setup for this suite of tests is diagramed in Figure 12. The cart and track system developed for the bifurcation tests was mounted to an electrodynamic shake table, with an NI c-DAQ I/O system used for all control and measurement acquisition. A 1 Ω, 10 W resistor was connected serially to the electromagnet coil to measure the current parameter, and a 68 kΩ, 0.25 W resistor was connected across the external leads of the inertial generator to measure the power output response.

Legend

① NI c-DAQ Module
② Electromagnet
③ Midé V22BL with tip magnet
④ Accelerometer
⑤ Electromagnet Coil Shunt Resistor, 1 Ω, 20 W
⑥ Energy Harvester Load Resistor, 68 kΩ, 0.25 W

Figure 12. Diagram of parametric study of dynamic response

The intent of this parametric study was to investigate the full bandwidth of resonant response frequencies for low-amplitude excitations with respect to the nonlinear buckling control parameter. Figure 13(a) to (b) shows the power output in the frequency domain for the maximum and minimum electromagnet coil current for up-chirp and down-chirp excitations, respectively. For the up-chirp excitation, a 3 Hz gap in resonance energy exists between the two coil current extrema. Figure 13(c) to (d) show that for discrete steps of the coil current, the transition of the resonant frequency peaks is continuous. To that extent, there exists an opportunity to capture vibration energy within an augmented range of frequencies with proper implementation of a control law on the electromagnet coil current.

Further insights into the continuity of the resonant frequency peaks and their relationship to the electromagnet coil current were also required for development of the open-loop control law described in the following sub-section. Figure 13(e) to (f) show that for relatively low coil current values, there is a nonlinear shift in the resonant frequency, and for higher coil current values the frequency shift plateaus. This nonlinear relationship is a result of the electromagnet core saturation effect, in which for low values of coil current has a greater net effect on the nonlinear

restoring force relative to current modulation when the core is saturated.

Open-loop control of bistable separatrix for augmented broadband response

This section details the design and implementation of an open-loop control law applied to the electromagnet coil in an effort to augment the broadband resonant frequency response of the inertial generator subject to harmonic chirp excitations.

The open-loop control signal was programmed to linearly modulate the electromagnet coil current in a manner that matches the peak power output across the range of frequencies shown in Figure 13(c) to (d). To accomplish this, the power response signal was enveloped, and the max value was extracted for each trial of the parametric sweep test. Since the measured data was stored as a vector array in Matlab, the index location of the max measured power is directly tied to the excitation frequency in the shake table. Figures 14(a) and (b) show the peak power points plotted as a function of the base excitation frequency along with an overlaid linear least-squares fit for both harmonic up-chirp and down-chirp excitations. The fitted line was then used as the modulating control signal for the
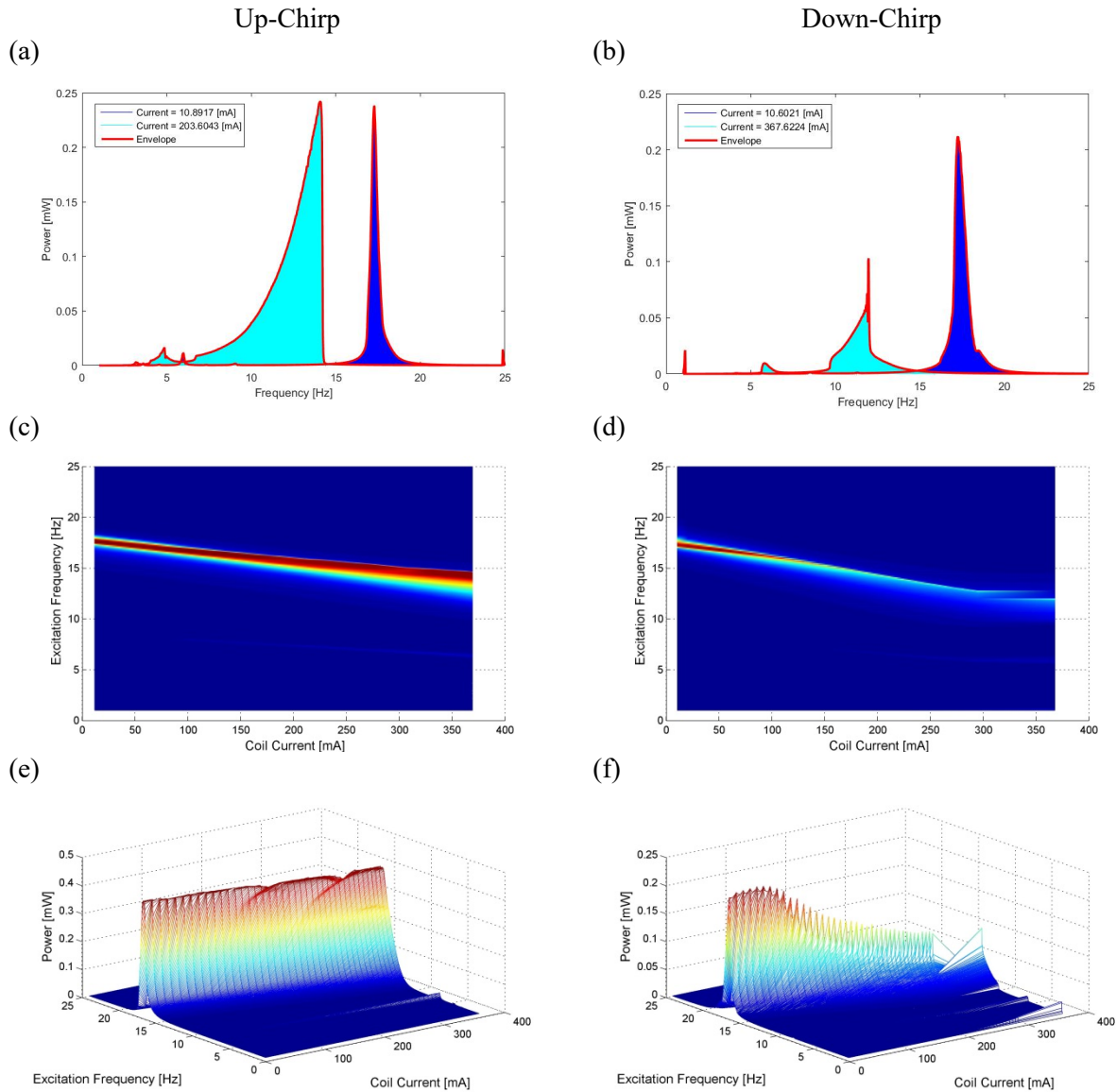
Figure 13. Output power of parametrically controlled inertial generator for harmonically excited chirp excitations.

transition region in the chirp excitation tests. While this control approach requires significant *a priori* knowledge of the parametric power response as the basis for its design, the focus of this initiative is to demonstrate the ability to augment the power output bandwidth by means of external coil current modulation.

As shown in Figures 14(c) and (d) the resulting output power response of the inertial generator now fully captures resonant energy in the transition region, thus validating the experimental hypothesis. As shown in Figure 14(d), the power

response for a down-chirp excitation is moderately less than that of the up-chirp excitation, which is primarily an artefact of the nonlinear resonance hysteresis exhibited in bistable oscillators.

Comparing the resonance bandwidth and total energy capture between conventional monostable and bistable schemes to the MIG system, it is clear that the MIG design is successful in augmenting vibration energy harvesting as shown in Table 3. The resonance bandwidth was calculated as the frequency range above 50% of peak power. However; since the MIG system
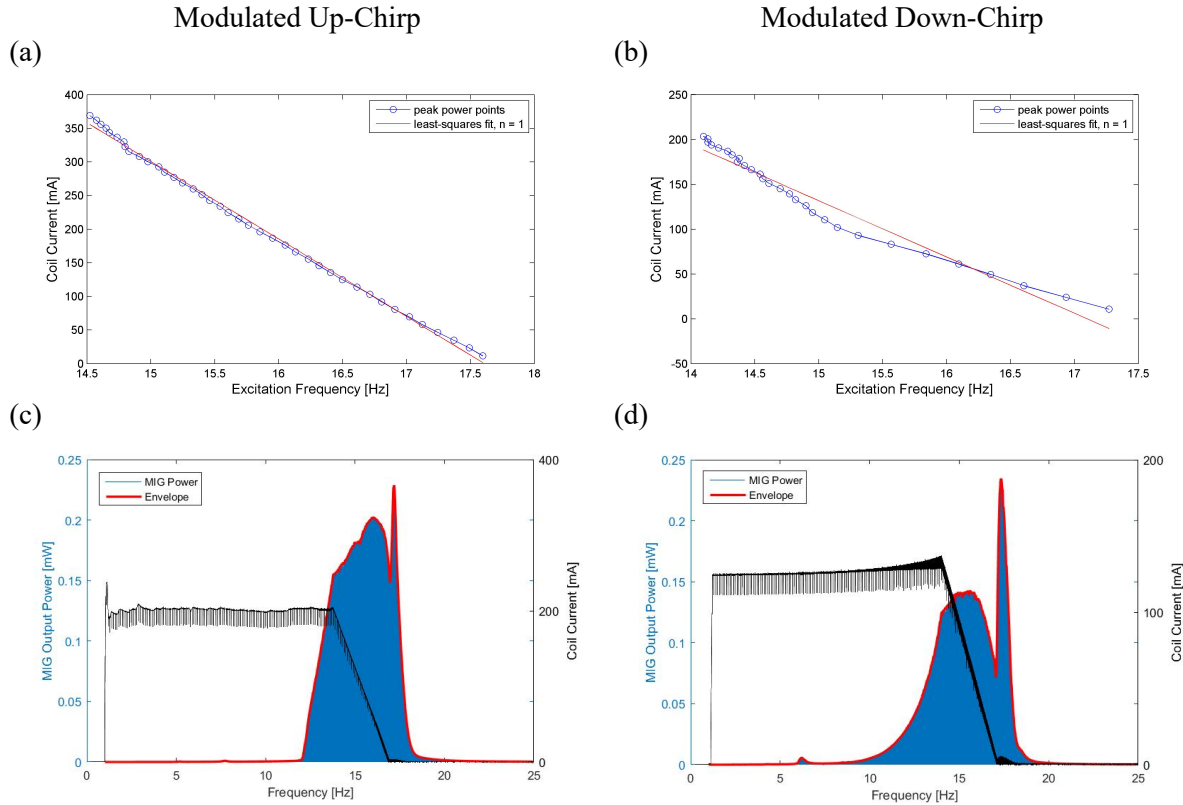
Figure 14. (a) Peak power points from up-chirp parametric excitation study with linear least-squares fit overlaid, (b) down-chirp peak power points with linear least-squares fit, (c) broadband power output of MIG energy harvester for up-chirp excitation, and (d) broadband power output of MIG for down-chirp excitation.

Table 3
Resonance bandwidth (Δf), total energy capture (E), and net energy balance (ΔE).

Parameter	Up-Chirp		Down-Chirp		Modulated	
	i_{coil_min}	i_{coil_max}	i_{coil_min}	i_{coil_max}	Up	Down
Δf	0.48 Hz	1.87 Hz	0.41 Hz	0.77 Hz	4.18 Hz	3.89 Hz
E_{total}	163 mJ	598 mJ	126 mJ	216 mJ	852 mJ	720 mJ
ΔE	--	--	--	--	-3690 mJ	-2552 mJ

requires active control of the buckling electromagnet, it is necessary to calculate the energy consumed by the control device. The measured coil resistance was 14 Ω, and the energy consumption of the electromagnet was calculated by integrating the measured DC power loss as a result of the applied coil current control shown in Figures 14 (c) and (d). In this regard, the MIG design demonstrated in this paper produces a negative energy balance, which adversely affects the possibility of field deployment. The net energy balance for the parametric studies was neglected

due to the fact that the monostable and bistable systems can be achieved passively using permanent magnets. As previously explored it the electromagnet power analysis section, this negative energy balance can potentially be rectified through an optimally designed buckling electromagnet. Furthermore, the open-loop control signal failed to capture the entire resonance bandwidth available.

Conclusions

This paper investigated a novel method of augmenting the resonant frequency bandwidth of bistable inertial generators by modulating the separatrix barrier height with a stationary electromagnet. Analytical models of the inertial generator and electromagnet were developed to study the parametric space in which the system transitions from linear to nonlinear behavior.

A quasi-static experimental test was conducted to validate the analytical bifurcation diagram, and a suite of dynamic tests were run to investigate the output power of the inertial generator subject to harmonic chirp excitations. Lastly, an augmented resonant frequency response was validated experimentally for low-amplitude chirp excitations by means of a linear, open-loop control law operating on the electromagnet coil current.

While the net energy balance was sub-optimal, the initial hypothesis was successfully verified. Future investigations into optimal buckling electromagnet designs and control signals have significant potential for creating a system that generates a net-positive energy balance while simultaneously expanding the broadband resonance bandwidth.

Acknowledgements

Appendix: Nonlinear Magnetic Potential Function

The nonlinear magnetic potential energy function derived in MATHEMATICA is as follows:

$$U_{mag} = \frac{\alpha_0(\alpha_1 \cos\theta + \alpha_2 \cos 2\theta + \alpha_3 \sin\theta + \alpha_4)}{\pi[\beta_0 + \beta_1 \cos\theta + \beta_2 \sin\theta + \omega[L,t]^2]^{5/2}} \quad (12a)$$

where

$$\alpha_0 = 2|\vec{\mu}_p||\vec{\mu}_{em}|\mu_0 \quad (12b)$$

$$\alpha_1 = -2(4a^2 + S^2) + 4\omega[L,t]^2 \quad (12c)$$

$$\alpha_2 = aS \quad (12d)$$

$$\alpha_3 = -4a\omega[L,t]\cos\theta \quad (12e)$$

$$\alpha_4 = S(7a + 6) \quad (12f)$$

$$\beta_0 = 4a^2 + S^2 \quad (12g)$$

$$\beta_1 = 4aS \quad (12h)$$

$$\beta_2 = 8a\omega[L,t] \quad (12i)$$

and $S = 4a + lc + 2s$, where a is the permanent magnet length, lc is the electromagnet core length, and s is the separation distance.

References

Derby N and Olbert S (2010) Cylindrical magnets and ideal solenoids. *American Journal of Physics* 78(3): 229–235.

Elvin N and Erturk A (2013) *Advances in energy harvesting methods*. Springer. Available from: http://books.google.com/books?hl=en&lr=&id=mLXv0uN4Th8C&oi=fnd&pg=PR5&dq=advances+in+energy+harvesting+methods&ots=OUkOgW_0pJ&sig=p96PN5Dd1aDEJUZnal5lzlIskJo (accessed 15 August 2013).

Erturk A and Inman DJ (2011) Broadband piezoelectric power generation on high-energy orbits of the bistable Duffing oscillator with electromechanical coupling. *Journal of Sound and Vibration* 330(10): 2339–2353.

Friswell MI, Ali SF, Bilgen O, et al. (2012) Non-linear piezoelectric vibration energy harvesting from a vertical cantilever beam with tip mass. *Journal of Intelligent*

Material Systems and Structures 23(13): 1505–1521.

Gao YJ, Leng YG, Fan SB, et al. (2014) Performance of bistable piezoelectric cantilever vibration energy harvesters with an elastic support external magnet. *Smart Materials and Structures* 23(9): 095003.

Harne RL and Wang KW (2013) A review of the recent research on vibration energy harvesting via bistable systems. *Smart Materials and Structures* 22(2): 023001.

Koplow MA, Bhattacharyya A and Mann BP (2006) Closed form solutions for the dynamic response of Euler–Bernoulli beams with step changes in cross section. *Journal of Sound and Vibration* 295(1–2): 214–225.

Leng YG, Gao YJ, Tan D, et al. (2015) An elastic-support model for enhanced bistable piezoelectric energy harvesting from random vibrations. *Journal of Applied Physics* 117(6): 064901.

Litak G, Friswell MI and Adhikari S (2010) Magnetopiezoelastic energy harvesting driven by random excitations. *Applied Physics Letters* 96(21): 214103.

Liu WQ, Badel A, Formosa F, et al. (2013) Novel piezoelectric bistable oscillator architecture for wideband vibration energy harvesting. *Smart Materials and Structures* 22(3): 035013.

Ouellette SA and Todd MD (2014) Broadband energy harvesting via adaptive control of bistable potential energy separatrix. In: Liao W-H (ed.), p. 90570Y. Available from: http://proceedings.spiedigitallibrary.org/proceeding.aspx?doi=10.1117/12.2044866 (accessed 14 May 2015).

Stanton SC and Mann BP (2010) On the dynamic response of beams with multiple geometric or material discontinuities. *Mechanical Systems and Signal Processing* 24(5): 1409–1419.

Stanton SC, McGehee CC and Mann BP (2010) Nonlinear dynamics for broadband energy harvesting: Investigation of a bistable piezoelectric inertial generator. *Physica D: Nonlinear Phenomena* 239(10): 640–653.

Su W-J, Zu J and Zhu Y (2014) Design and development of a broadband magnet-induced dual-cantilever piezoelectric energy harvester. *Journal of Intelligent Material Systems and Structures* 25(4): 430–442.

Virgin LN (2007) *Vibration of axially-loaded structures*. Cambridge University Press. Available from: http://books.google.com/books?hl=en&lr=&id=1EsTSh-Tw0UC&oi=fnd&pg=PR15&dq=info:UIj9w01J-BYJ:scholar.google.com&ots=uKLGBApk5F&sig=EtqJOdqFK6AckLxCdBtx9GNAZ3c (accessed 10 January 2016).

Virgin LN, Plaut RH and Cheng C-C (1992) Prediction of escape from a potential well under harmonic excitation. *International Journal of Non-Linear Mechanics* 27(3): 357–365.

Yung KW, Landecker PB and Villani DD (1998) An Analytic Solution for the Force Between Two Magnetic Dipoles. *Magnetic and Electrical Separation* 9(1): 39–52.

Zhu D and Beeby SP (2013) A broadband electromagnetic energy harvester with a coupled bistable structure. *Journal of Physics: Conference Series* 476(1): 012070.

Zhu Y and Zu J (2014) A magnet-induced buckled-beam piezoelectric generator for wideband vibration-based energy harvesting. *Journal of Intelligent Material Systems and Structures*: 1045389X14541498.